

# Rb₃Er₄Cu₅Te₁₀: Exploring the Frontier between Polar Intermetallics and Zintl-Phases via Experimental and Quantumchemical Approaches

Fabian C. Gladisch,<sup>[a]</sup> Jan van Leusen,<sup>[a]</sup> Marco T. Passia,<sup>[a, c]</sup> Paul Kögerler,<sup>[a, b]</sup> and Simon Steinberg\*<sup>[a]</sup>

The tailored design of solid-state materials requires a proper understanding of their respective electronic structures. In order to rationalize the relationships between crystal structures and electronic structures in intermetallic compounds, the Zintl-Klemm concept has been frequently employed. Yet, the frontier between the valence-electron concentrations (e/a) of the Zintl-and the polar intermetallic phases has remained unclear to date. To shed some light on this frontier, we explored the

electronic structure of the quaternary compound  $Rb_3Er_4Cu_5Te_{10}$ . To this effect, the crystal structure of this telluride, which was obtained as pure phase from high-temperature reactions, was determined by means of X-ray diffraction experiments for the very first time. In addition, the magnetic properties of the  $Rb_3Er_4Cu_5Te_{10}$  were also determined in order to explore the erbium 4f states in more detail.

## Introduction

In the guest for new materials suited for emerging applications, chalcogenides have received an enormous attraction among scientists, [1] because the characteristics of several chalcogenides place them at the cutting edge of basic research and qualify them for uses in diverse technical applications. For instance, most recent research on chalcogenides included explorative efforts on thermoelectrics, [2] rewriteable data storage media, [3] topological insulators,  $^{[4]}$  and charge density waves  $^{[5]}$  – to name only a few. In the context of the design of new materials, a thorough knowledge of the electronic structures is also required, because the interpretation of the electronic structure allows us to understand and to forecast materials' properties. [6] To recognize the relationships between the crystal and electronic structures of tellurides, the valence-electron distributions of the constituents have frequently been interpreted by applying the Zintl-Klemm<sup>[8]</sup> concept. Within the framework of this formalism, the valence electrons are (formally) transferred from the more electropositive to the more electronegative atoms, and the latter constitute polyanions that are isostructural to the structural motifs of isoelectronic elements.

Most recent research on the electronic structures of tellurides showed that the bonding nature of the tellurides, which solely comprise s-block elements, should be depicted as ionic, i.e. fully in line with the predictions based on the applications of the Zintl-Klemm concept. Additional research on tellurides that mainly contain p-block elements and belong to the family of the incipient metals<sup>[10]</sup> were reported to show a remarkable electronic state at the frontier between entire valence-electron delocalization and localization. Yet, the electronic structures of tellurides belonging to the family of the incipient metals cannot be understood by means of any valence-electron counting schemes.[11] Likewise, valence-electron rules do not apply to the members of the family of the polar intermetallics, whose crystal structures are composed of polyanionic or -cationic fragments accompanied by monoatomic counterions.[12] Most recent research[13] on tellurides containing transition metals showed that these attributes of polar intermetallics also apply to these tellurides, which accordingly should be assigned to the class of the polar intermetallic compounds. Yet, is there a frontier between polar intermetallics and Zintl phases with regard to the valence-electron concentrations (e/a)?

Indeed, the e/a-values reported<sup>[14]</sup> for the existence ranges of polar intermetallics and Zintl phases vary widely. To answer this question, we examined the electronic structure of the quaternary telluride Rb<sub>3</sub>Er<sub>4</sub>Cu<sub>5</sub>Te<sub>10</sub>, whose e/a-value (3.64) is located in the questionable e/a region. To do so, we also determined the crystal structure and magnetic properties of this quaternary telluride, which was obtained from high-temperature solid-state reactions for the very first time.

[a] F. C. Gladisch, Dr. Dr.-Ing. J. van Leusen, M. T. Passia, Prof. Dr. P. Kögerler, Dr. S. Steinberg

Institute of Inorganic Chemistry, RWTH Aachen University,

Landoltweg 1, 52074 Aachen, Germany

 $\hbox{\it E-mail: simon.steinberg@ac.rwth-aachen.de}$ 

https://www.ac.rwth-aachen.de/extern/steinberg/index.php

[b] Prof. Dr. P. Kögerler Peter Grünberg Institute – PGI-6, Research Centre Jülich,

52425, Jülich, Germany [c] M. T. Passia

Present address: Institute of Organic Chemistry, RWTH Aachen University,

Landoltweg 1, 52074 Aachen, Germany

Supporting information for this article is available on the WWW under https://doi.org/10.1002/ejic.202100795

© 2021 The Authors. European Journal of Inorganic Chemistry published by Wiley-VCH GmbH. This is an open access article under the terms of the Creative Commons Attribution License, which permits use, distribution and reproduction in any medium, provided the original work is properly cited.



## **Results and Discussion**

The quaternary telluride was obtained from high-temperature reactions of the elements erbium, copper, and tellurium in the presence of the reactive flux<sup>[15]</sup> RbCl acting both as a solvent as well as a reactant. Rb<sub>3</sub>Er<sub>4</sub>Cu<sub>5</sub>Te<sub>10</sub> was obtained as single phase and was subsequently examined with regard to its crystal structure, magnetic properties and electronic structure (see Experimental Details Section for further details on syntheses, collections of the experimentally accessible data and electronic structure computations).

#### **Structural Details and Magnetic Properties**

To date, three different structure types have been determined<sup>[16]</sup> to crystallize with the net composition  $A_3R_4Cu_5Te_{10}$  (A=alkali metal; R=rare-earth element; Z=2) and the space group *Pnnm* (no. 58; Pearson symbol oP44). Among the diverse A<sub>2</sub>R<sub>4</sub>Cu<sub>5</sub>Te<sub>10</sub> types of structure, the crystal structure of each representative is composed of the same sort of tellurium network enclosing the alkali metal, rare-earth and copper atoms. The tellurium polyhedra, which encompass the respective alkali metals, rareearth elements and copper atoms, are condensed via common vertices, edges, and faces to chains parallel to the crystallographic axis with the shortest translation period that is, in principle, the c axis; however, a different lattice setting has been chosen for K<sub>3</sub>Dy<sub>4</sub>Cu<sub>5</sub>Te<sub>10</sub>. In the following, we will use the lattice setting employed for most representatives of these structure types for the benefit of better comparisons. The crystal structures of each A<sub>3</sub>R<sub>4</sub>Cu<sub>5</sub>Te<sub>10</sub> type comprise five independent tellurium sites, two different rare-earth positions, and two independent alkali metal positions that correspond to the same Wyckoff sites (Te: 4q; R: 4q; A: 4q/2a; K<sub>3</sub>Dy<sub>4</sub>Cu<sub>5</sub>Te<sub>10</sub>: 4q/ 2c) and two independent copper sites (Cu1 and Cu2; Wyckoff positions 4q, 4q) showing similar coordination environments. Yet, the crystal structures of the three A<sub>3</sub>R<sub>4</sub>Cu<sub>5</sub>Te<sub>10</sub> types differ in one significant aspect: the respective locations of the Cu3 sites (Wyckoff position 4g). In the quaternary  $K_3R_4Cu_5Te_{10}$  (R= Sm, Gd, Er), the Cu3 atoms are located in the near of the A1 atoms (see Figure S1, Supporting Information), while the Cu3 atoms reside close to the Cu2 atoms in the crystal structures of  $Rb_3R_4Cu_5Te_{10}$  (R = Nd, Gd) and  $Cs_3Gd_4Cu_5Te_{10}$  (Figure 1). Because

Table 1. Details of the crystal structure investigations and refinements for  $Rb_3Er_4Cu_5Te_{10}$ . Rb<sub>2</sub>Er<sub>4</sub>Cu<sub>5</sub>Te<sub>10</sub> formula weight 2519.15 space group Pnnm (no. 58) a, Å 17.111(4) b, Å 17.455(4) *c*, Å 4.329(1) volume, Å<sup>3</sup> 1292.9(5) density (calc.), g/cm3 6.471 μ, mm 33.505 F(000)2096  $\theta$  range,  $^{\circ}$ 2.33-25.79  $-20 \le h \le 18$ index ranges  $-21 \le k \le 17$ -5≤*l*≤5 no. of reflns collected 7312 no. of indep reflns/R<sub>int</sub> 1419/0.108 no. of reflns  $I > 2\sigma(I)/R_a$ 1029/0.092 refinement method full matrix on least squares on F2 data/restraints/parameters 1419/0/71 GOF on  $F^2$ 1.02 final R indices  $[F^2 > 2\sigma(F^2)]$  $R_1 = 0.046$ ,  $wR_2 = 0.097$  $R_1 = 0.075, wR_2 = 0.104$ R indices (all data) largest diff peak and hole, e-/Å3 3.28 and -3.10

copper atoms are distributed on both of the aforementioned Cu3 sites corresponding to Cu3 and Cu4 positions in the crystal structure of  $K_3Dy_4Cu_5Te_{10}$ , this type of structure can be viewed at as an intermediate of the aforementioned  $A_3R_4Cu_5Te_{10}$  types. The herein reported  $Rb_3Er_4Cu_5Te_{10}$  is isostructural with  $Rb_3R_4Cu_5Te_{10}$  (R=Nd, Gd) and  $Cs_3Gd_4Cu_5Te_{10}$ , and a closer description of its crystal structure (Table 1 and Table 2) will be provided in the following.

The Rb1 atoms are surrounded by seven tellurium atoms assembling monocapped trigonal prisms, [Rb@Te<sub>7</sub>], while the Rb2 atoms residing at the vertices and the centers of the unit cell are coordinated by tellurium atoms in a cubic fashion, [Rb@Te<sub>8</sub>] (Figure 1). Furthermore, each [Rb@Te<sub>7</sub>] unit is connected to the nearest-neighbor [Rb@Te<sub>7</sub>] clusters within a given chain via the triangular bases, while one square face of each [Rb@Te<sub>7</sub>] unit is shared with a tellurium cube of the nearest [Rb@Te<sub>7</sub>] chain in the sequence [Rb@Te<sub>7</sub>]—[Rb@Te<sub>8</sub>]—[Rb@Te<sub>7</sub>]. The Rb—Te distances in the [Rb@Te<sub>7</sub>] and [Rb@Te<sub>8</sub>] units (3.514(3) Å–3.844(2) Å) scale in the same range as those

Atom	Position	X	у	Z	$U_{\rm iso}/U_{\rm eq}$ , ${ m \AA}^2$	Occ. (< 1)
Er1	4 <i>g</i>	0.4354(1)	0.7818(1)	1/2	0.0155(3)	
Er2	4 <i>g</i>	0.2109(1)	0.5565(1)	1/2	0.0163(3)	
Te1	4 <i>g</i>	0.0881(1)	0.6106(1)	0	0.0157(4)	
Te2	4 <i>g</i>	0.2778(1)	0.7132(1)	1/2	0.0162(4)	
Te3	4 <i>g</i>	0.1258(1)	0.3988(1)	1/2	0.0146(4)	
Te4	4 <i>g</i>	0.4974(1)	0.6819(1)	0	0.0159(4)	
Te5	4 <i>g</i>	0.3176(1)	0.5015(1)	0	0.0159(4)	
Cu1	4 <i>g</i>	0.3450(2)	0.6508(2)	0	0.0259(8)	
Cu2	4 <i>g</i>	0.0613(2)	0.4600(2)	0	0.0239(8)	
Cu3	4 <i>g</i>	0.0251(5)	0.5485(5)	1/2	0.051(2)	0.5
Rb1	4 <i>g</i>	0.1683(2)	0.8300(2)	0	0.0231(6)	
Rb2	2a	0	0	0	0.0293(9)	



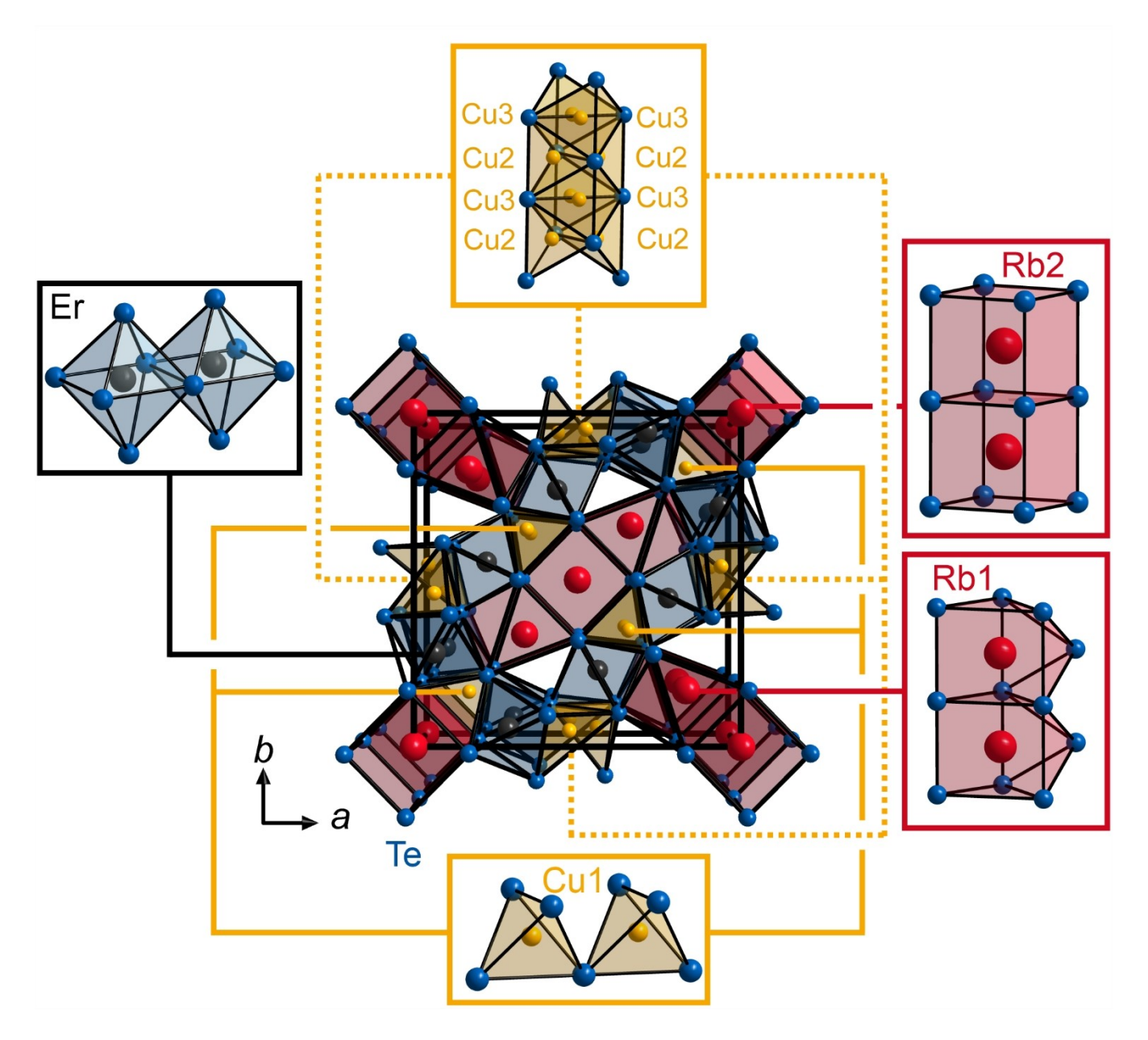


Figure 1. Representation of the crystal structure of  $Rb_3Er_4Cu_5Te_{10}$  viewed along the *c* axis: the diverse types of tellurium polyhedra surrounding the rubidium, erbium, and copper atoms are shown in the diverse insets.

observed for the previously reported rubidium-containing  $A_3R_4Cu_5Te_{10}$  compounds. [16a] Each [Rb@Te\_8] unit is connected via opposite square faces to the nearest-neighbor units within a given [Rb@Te\_8] chain and via four common edges to four tellurium octahedra, which surround the [Rb@Te\_8] fragments and encapsulate the erbium atoms, [Er@Te\_6]. In addition, each [Rb@Te\_7] unit shares two vertices, three edges, and one face with the nearest neighboring [Er@Te\_6] units such that each [Rb@Te\_7] agglomerate is surrounded by six [Er@Te\_6] octahedra. Each [Er@Te\_6] unit is linked via two opposite edges to neighboring [Er@Te\_6] units within a given linear  $\frac{1}{\infty}$  [Er@Te\_6] chain, which is interconnected via common vertices to adjacent  $\frac{1}{\infty}$  [Er@Te\_6] chains.

The copper atoms are embedded in the voids enclosed by the  $\frac{1}{\infty}[\text{Er@Te}_6]$ , the  $\frac{1}{\infty}[\text{Rb@Te}_7]$ , and the  $\frac{1}{\infty}[\text{Rb@Te}_8]$  chains, and are tetrahedrally coordinated by tellurium atoms. The tellurium tetrahedra occupied by the Cu1 atoms are condensed via common vertices in  $\frac{1}{\infty}[\text{Cu@Te}_4]$  chains along (001), while the tellurium tetrahedra encapsulating the Cu2 and Cu3 atoms are connected via common edges to  $\frac{1}{\infty}[\text{Cu@Te}_4]$  double chains (Figure 1). Under consideration of the atomic covalent radius of copper (1.32 Å),[17] the Cu—Cu separations (2.521(5) Å–2.731(6) Å) within the  $\frac{1}{\infty}[\text{Cu@Te}_4]$  double chains point to potential Cu—Cu interactions,[18] yet, a chemical bonding analyses based on first-principles-based methods (below) is required to verify this prediction. Notably, the analysis of the



initial structure models for the herein reported tellurides also revealed extremely short Cu3—Cu3 contacts (1.90(1) Å), which cannot be considered as a reasonable Cu—Cu distance and, hence, provided further proof to the presence of positional disorder for the Cu3 sites (see Structure Determination section).

The SQUID magnetometry data (Figure 2) for Rb<sub>3</sub>Er<sub>4</sub>Cu<sub>5</sub>Te<sub>10</sub> clearly show a temperature-dependence of the magnetic susceptibility. The  $\chi_m T$  value of about 43.6 cm<sup>3</sup> K mol<sup>-1</sup> is slightly smaller than the theoretical value<sup>[19]</sup> (45.9 cm<sup>3</sup> Kmol<sup>-1</sup>) expected for four non-interacting erbium cations with  ${}^4I_{15/2}$  ground terms. This is primarily due to the fact that the theoretical  $\chi_{\rm m}T$  values typically<sup>[19b]</sup> disregard minor contributions arising from excited states that mix with the ground states. Additionally, this outcome agrees well with the results of the magnetic properties measurements<sup>[20]</sup> for different erbium-containing tellurides showing only weak crystal field effects for such materials. These data also indicate that the erbium 4f electrons are rather localized. Because such localized states cannot be involved in Er-Te bonding, the erbium 4f states could be treated as corelike in the density-functional-theory-based bonding analysis of Rb<sub>3</sub>Er<sub>4</sub>Cu<sub>5</sub>Te<sub>10</sub>.

#### **Electronic Structure and Bonding Analysis**

An application of the Zintl-Klemm concept to the quaternary telluride proposes an electron-precise valence-electron distribution according to the formula  $(Rb^+)_3(Er^{3+})_4(Cu^+)_5(Te^{2-})_{10}$ . And yet, there are certain peculiarities in the crystal structure of the quaternary telluride, e.g., the disordered Cu positions or the close Cu–Cu separations (see above), which cannot be understood by applying the aforementioned formalism. As the relationship between the structural features and the electronic structures cannot be recognized by applying (any) straightforward valence-electron rules, the electronic structure of  $Rb_3Er_4Cu_5Te_{10}$  was examined using first-principles-based means to account for the aforementioned peculiarities. Because the

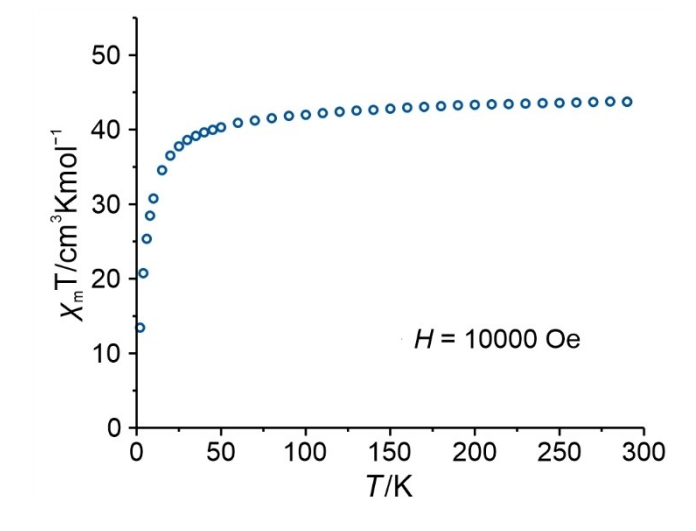


**Figure 2.** Temperature dependence of  $\chi_{\rm m}T$  for Rb<sub>3</sub>Er<sub>4</sub>Cu<sub>5</sub>Te<sub>10</sub> measured at  $H\!=\!10$  kOe.

crystal structure of Rb<sub>3</sub>Er<sub>4</sub>Cu<sub>5</sub>Te<sub>10</sub> comprises one positionally disordered copper site (see Table 2) that is not suited as a starting parameter for the electronic structure calculations, the density-functional-theory-based computations had to be accomplished for two "Rb<sub>3</sub>Er<sub>4</sub>Cu<sub>5</sub>Te<sub>10</sub>" models (in the following, the hypothetical structures will be denoted by the quotation marks). The two hypothetical "Rb<sub>3</sub>Er<sub>4</sub>Cu<sub>5</sub>Te<sub>10</sub>" structure models were developed based on the two possible structural configurations for the telluride such that the "Rb<sub>3</sub>Er<sub>4</sub>Cu<sub>5</sub>Te<sub>10</sub>" models approximate the experimentally observed Rb<sub>3</sub>Er<sub>4</sub>Cu<sub>5</sub>Te<sub>10</sub> crystal structure (see Figure S4 for further details). The analyses of the electronic band structure and the bonding situation were accomplished for the "Rb<sub>3</sub>Er<sub>4</sub>Cu<sub>5</sub>Te<sub>10</sub>" model 2 which corresponds to the lowest total energy and, hence, is the most preferable "Rb<sub>3</sub>Er<sub>4</sub>Cu<sub>5</sub>Te<sub>10</sub>" model to compare to the experimentally determined structure model.[21] Because the difference between the total energies of two inspected "Rb<sub>3</sub>Er<sub>4</sub>Cu<sub>5</sub>Te<sub>10</sub>" models (0.2 kJ/mol) is in the range of the used reaction temperatures (900 °C), it can be inferred that the disorder of the Cu3 sites is a consequence of a non-equilibrium condensation into the solid state.

An examination of the electronic band structure for the "Rb $_3$ Er $_4$ Cu $_5$ Te $_{10}$ " model 2 (Figure 3) reveals that the Fermi level,  $E_{\text{F}}$ , falls in a direct band gap of 0.57 eV which indicates that this telluride should be a semiconductor. Furthermore, the location of the Fermi level in a band gap suggests that an electronically favorable situation<sup>[22]</sup> is attained for Rb<sub>3</sub>Er<sub>4</sub>Cu<sub>5</sub>Te<sub>10</sub>. A closer inspection of the electronic band structures and the densitiesof-states (DOS) curves bares that the states near  $E_{\rm F}$  in the "Rb<sub>3</sub>Er<sub>4</sub>Cu<sub>5</sub>Te<sub>10</sub>" model 2 originate to a great extent from the Cud atomic orbitals beside certain contributions from the Te-p atomic orbitals. Accordingly, it can be inferred that the Cu-d as well as Te-p states play an important role in the bonding interactions located in the energy regions near the Fermi level. To provide an insight into the bonding situation of the "Rb<sub>3</sub>Er<sub>4</sub>Cu<sub>5</sub>Te<sub>10</sub>" model 2, we followed up with an examination of the crystal orbital Hamilton population curves (Figure 3c) and their respective integrated values (ICOHP; Table 3). In this context, the cumulative -ICOHP/cell values, i.e., the sum of all -ICOHP/bond values of a given interaction within a unit cell, were projected as percentages to the net bonding capabilities to evaluate the contributions from the diverse sorts of interatomic contacts to the net bonding - a procedure that has been largely employed elsewhere. [12b,23]

An examination of the —COHP curves and the respective integrated values (Table 3) for the "Rb<sub>3</sub>Er<sub>4</sub>Cu<sub>5</sub>Te<sub>10</sub>" model 2 (Figure 3) reveals that the Rb—Te contacts are weakly bonding as mirrored by the relatively small —ICOHP/bond values ranging from 0.0683 to 0.0261 eV/bond. Such small —ICOHP/bond values are typically an attribute of bond types corresponding to a less bonding (covalent) character like rather delocalized metal-metal bonds or ionic bonds between closed-shell species. Under consideration of the electronegativities<sup>[24]</sup> of Rb (0.89) and Te (2.01), it is clear that the weakly bonding character of the Rb—Te interactions reflects the ionic nature of these heteroatomic bonds. In addition to these heteroatomic interactions, there also significant Er—Te as well as Cu—Te bonding interactions



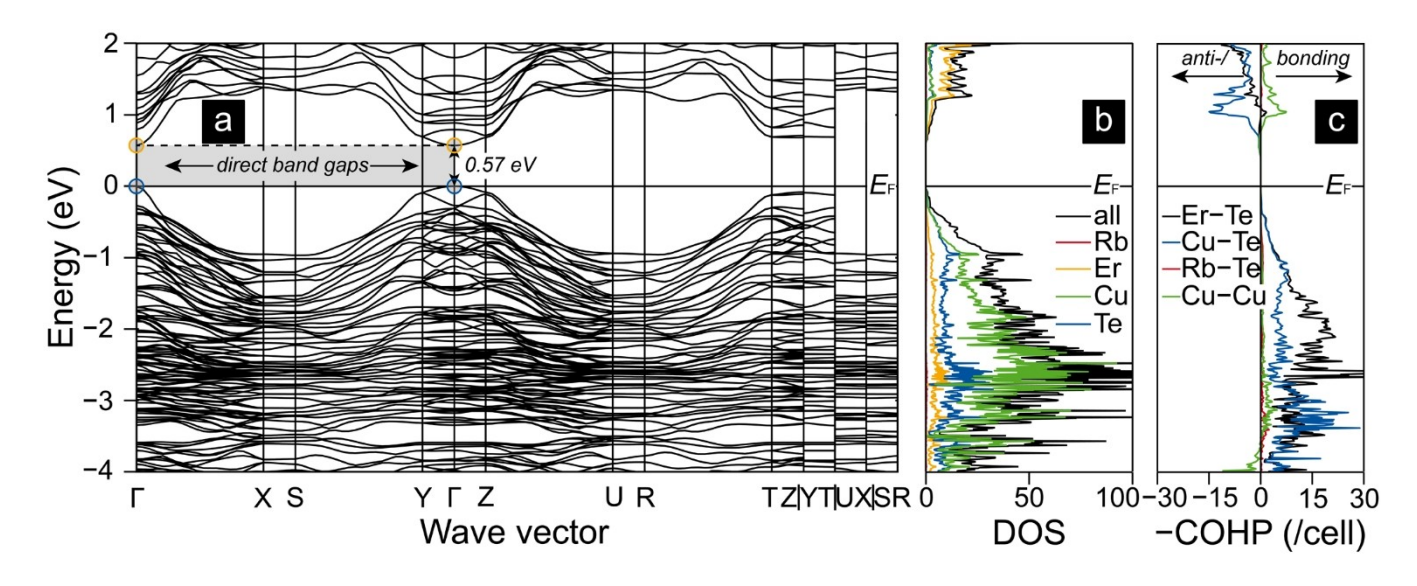


Figure 3. (a) Electronic band structure, (b) density-of-states (DOS), and (c) Crystal Orbital Hamilton Population (COHP) curves of the "Rb<sub>3</sub>Er<sub>4</sub>Cu<sub>5</sub>Te<sub>10</sub>" model 2 corresponding to the lowest total energy: the Fermi level, *E*<sub>F</sub>, is represented by the black horizontal line, while atom- and orbital-projected DOS curves may be extracted from the Supporting Information (Figure S5).

Table 3. Distance as well as -ICOHP/bond ranges, average -ICOHP/bond values, cumulative -ICOHP/cell values, and percentages of the cumulative -ICOHP/cell values to the net bonding capability in the "Rb<sub>3</sub>Er<sub>4</sub>Cu<sub>5</sub>Te<sub>10</sub>" model 2. Distances and the respective -ICOHP/bond values of selected interactions may be extracted from the Supporting Information (Table S6).

Interaction	Distances ranges [Å]	<pre>—ICOHP/bond (eV/bond)</pre>	ave. —ICOHP/bond (eV/bond)	cum. –ICOHP per cell	[%]
Er–Te	2.959-3.287	1.6841-0.7214	1.1687	56.0963	43.56
Cu–Te	2.646-2.967	2.0224-0.8110	1.6054	64.2188	49.87
Rb–Te	3.532-3.915	0.0683-0.0261	0.0486	2.1401	1.66
Cu-Cu	2.498-2.686	0.7359-0.5902	0.6320	6.3201	4.91

below the Fermi level,  $E_{\rm F}$ . In the case of the Er–Te contacts, the -ICOHP/bond values range between 1.6841 and 0.7214 eV per bond and contribute 43.56% to the total bonding capabilities, while the Cu-Te -ICOHP/bond values reach from 2.0224 to 0.8110 eV/bond and contribute 49.87% to the net bonding. Accordingly, the majority of the bonding populations resides between the Er-Te as well as Cu-Te separations, which show a much more bonding character than the Rb-Te interactions. Such a strongly bonding character means that the valenceelectrons must be distributed in the Cu-Te and Er-Te separations like in covalent bonds. Yet, the electronegativities<sup>[24]</sup> of Er (1.11), Cu (1.75) and Te (2.01) indicate that there must be a certain valence-electron transfer from the copper and erbium to the tellurium atoms such that the Cu-Te and Er-Te bonds should be classified as polar-covalent. These classifications are in good agreement with most recent research on the bonding situations in tellurides comprising transition-metals (see Introduction). The Cu-Cu -ICOHP/bond values (Table 3) are clearly indicative of a net bonding character for these homoatomic interactions; however, the Cu-Cu -ICOHP/bond values solely contribute 4.91% to the gross bonding capability of the "Rb<sub>3</sub>Er<sub>4</sub>Cu<sub>5</sub>Te<sub>10</sub>" model 2 because of the small amounts of Cu-Cu contacts. Furthermore, these homoatomic interactions correspond to smaller -ICOHP/bond values than the Er-Te and

Cu—Te interactions, as the former homoatomic interactions change from bonding to antibonding states below the Fermi level (Figure 3) – a circumstance that is typically [18c] encountered for  $d^{10}$ — $d^{10}$  interactions.

## **Conclusions**

In case of solid-state materials, three broad and different classes of intermetallics, i.e. the Hume-Rothery phases, the polar intermetallic phases and the Zintl phases, have been established based on structural features, the electronic structures and the physical properties. While the frontier between the two former families of intermetallics is well determined based on the valence-electron concentrations (e/a), yet, there is no well-defined e/a-frontier between the two latter classes of intermetallics. Therefore, the electronic structure was examined for a quaternary alkali metal rare-earth copper telluride, i.e. Rb<sub>3</sub>Er<sub>4</sub>Cu<sub>5</sub>Te<sub>10</sub>, whose e/a value is located in the cross-border region of polar intermetallic and Zintl phases.

Herein, we have discussed the crystal structure of the quaternary telluride, which was obtained from high-temperature solid-state syntheses. The crystal structure of this quaternary telluride is composed of different chains of tellurium



polyhedra enclosing the rubidium, copper and erbium atoms. In addition to the crystal structure determinations, the magnetic properties of Rb<sub>3</sub>Er<sub>4</sub>Cu<sub>5</sub>Te<sub>10</sub> were also examined, and the outcome of these measurements justify treating the erbium 4f electrons as core-like in all density-functional-theory-based computations. An application of the Zintl-Klemm concept to this telluride proposes an electron-precise valence-electron distribution according to the formula (Rb<sup>+</sup>)<sub>3</sub>(Er<sup>3+</sup>)<sub>4</sub>(Cu<sup>+</sup>)<sub>5</sub>(Te<sup>2-</sup>)<sub>10</sub>. Yet, the relationships between the structural features and the electronic structure of Rb<sub>3</sub>Er<sub>4</sub>Cu<sub>5</sub>Te<sub>10</sub> cannot be understood by applying any valence-electron rules. The results of the guantum-chemical examinations indicate that the positional disorder of one copper position is a consequence of a non-equilibrium condensation into the solid state. A bonding analysis for a "Rb<sub>3</sub>Er<sub>4</sub>Cu<sub>5</sub>Te<sub>10</sub>" model approximating the actual crystal structure of the telluride revealed that most of the bonding populations are located in the Er-Te and Cu-Te contacts. These heteroatomic interactions should be classified as polar-covalent, while the Rb-Te bonds were categorized as ionic. Furthermore, homoatomic Cu-Cu bonding was shown to be a minor, but evident factor in overall bonding. Accordingly, the quaternary telluride is composed of a polar-covalently bonded network that consists of the copper, erbium and tellurium atoms and is reduced by the rubidium cations. Under consideration of this description and the lack of any applicable valence-electron rules, Rb<sub>3</sub>Er<sub>4</sub>Cu<sub>5</sub>Te<sub>10</sub> fulfills attributes of polar intermetallic compounds and should be assigned to this family of compounds. Although the application of the Zintl-Klemm formalism provides certain (correct) hints regarding the distributions of the valence-electrons in this quaternary telluride, yet, this treatment should be handled with caution in the present case.

# **Experimental Section**

#### **Synthesis**

Pure phase Rb<sub>3</sub>Er<sub>4</sub>Cu<sub>5</sub>Te<sub>10</sub> was obtained from reactions of 129.1 mg erbium (smart elements®, Vienna, Austria; 99.99%), 49.0 mg copper (smart elements<sup>®</sup>; > 99.5 %), 205.2 mg tellurium (Merck<sup>®</sup>, Darmstadt, Germany; > 99%), and 116.7 mg rubidium chloride (Sigma Aldrich®, St. Louis, USA; 99.8%). Prior to its usage, traces of water were removed from the rubidium chloride under a reduced atmosphere, while powders of erbium were obtained from filing ingots whose surfaces were polished prior to every use. The reaction mixtures were weighed in the aforementioned ratio, then homogenized, and finally loaded into fused-silica tubes, which were closed using quick-fit tubing adapters. To prevent any contaminations of the samples by air or moisture, all these sample preparations were accomplished under a dry argon atmosphere within a glove box (MBraun®, Garching, Germany;  $H_2O < 0.1$  ppm by volume;  $O_2 <$ 0.1 ppm by volume). The fused-silica tubes were subsequently flame-sealed under a dynamic vacuum of at least 2×10<sup>-3</sup> mbar, and the samples were heated using computer-controlled tube furnaces and the following temperature program: heat to 900 °C with a rate of 80 °C/h, keep that temperature for one week, cool to 300 °C with rate of 5 °C/h and equilibrate to room temperature within three hours. After the samples had been taken out of the furnaces, the obtained products were thoroughly washed with methanol to remove the excess rubidium chloride and further byproducts. The product appeared as a grey powder containing black crystals of cuboid shape and was stable against exposure to air and water at room temperature for at least several weeks. Phase analyses based on examinations of the powder X-ray diffraction patterns collected for the samples revealed that the quaternary telluride was obtained as pure phase (see Figure S1).

#### **Structure Determination**

Samples considered for single-crystal X-ray (SCXR) diffraction experiments were selected from the bulk materials and fixed on glass fibers with grease. The mounted samples were transferred to a Bruker® APEX CCD diffractometer (Bruker Inc., Madison, WI; Mo Kα radiation,  $\lambda = 0.71073$  Å), which was employed for initial inspections of the quality of the selected samples as well as the collections of the SCXR intensity data sets at room temperature. After indexing the SCXR intensity data sets, a primitive orthorhombic lattice was identified based on the full data set. Subsequently, the SAINT+ and SADABS software<sup>[25]</sup> packages were used for the integrations of the raw SCXR intensity data and the multi-scan absorption corrections. respectively. Applications of the reflection conditions to the SCXR intensity data sets were accomplished with the aid of the XPREP algorithms within the APEX2<sup>[26]</sup> suite, and clearly pointed to the orthorhombic space group Pnnm (no. 58), which was chosen for the structure solution and refinements. The crystal structure was solved using direct methods (SHELXS-97), while all least-squares refinements on  $F^2$  which also included anisotropic atomic displacement parameters were carried out with the SHEXL[27] code. An examination of the coordination environments for all atomic positions revealed the presence of extremely short Cu3-Cu3 contacts (~ 2.0 Å) which were too small as to be considered as Cu-Cu bonds with regard to the atomic covalent radius of copper (1.32 Å).[17] Furthermore, the anisotropic atomic displacement parameters corresponding to the Cu3 sites were much larger than those observed for the remaining copper sites. Because these analyses strongly indicated the occurrence of positional disorder for the Cu3 sites, these copper positions were refined as positionally disordered sites in subsequent cycles of refinements. Additional topological analyses of the refined structure models did not provide any hints to a space group being different from Pnnm which was also corroborated by applying the ADDSYM algorithm within the PLATON<sup>[28]</sup> code. Details regarding the crystal structure investigations and refinements are provided in the Table 1, while the atomic positions and equivalent isotropic displacement parameters are listed in the Table 2.

#### **Characterization Methods**

Powder X-ray Diffractometry: To identify the constituents of the obtained samples, the powder X-ray diffraction (PXRD) patterns which were observed for the diverse samples were compared to those simulated for the quaternary telluride and feasible sideproducts. For the collections of the PXRD patterns, the samples were first pestled and, then, dispersed on acetal sheets with grease, which were fixed between aluminum rings. The sets of PXRD data were collected for all obtained samples using a STOE® StadiP diffractometer at room temperature (Stoe & Cie® GmbH, Darmstadt, Germany: area detector, Cu K $\alpha$  radiation:  $\lambda = 1.54059$  Å). The data collections and analyses were carried out with the aid of the WinXPow[29] software package, while the phase analyses were completed utilizing the Match! software package.[30] Rietveld refinements based on the PXRD patterns of the obtained product were completed using the FullProf<sup>[31]</sup> suite within the WinPLOTR<sup>[32]</sup> environment, and the results of the refinements may be extracted from the Supporting Information.



Magnetic Measurements: The magnetic properties of the quaternary telluride were determined employing a Quantum Design MPMS-5XL SQUID Magnetometer (Quantum Design, Darmstadt, Germany). To prepare the sample for the measurements 47.34 mg of Rb<sub>3</sub>Er<sub>4</sub>Cu<sub>5</sub>Te<sub>10</sub> were first finely ground and, then, sealed in a PTFE capsule. The acquired data were corrected for the diamagnetic contributions of the sample holder and the compound. The temperature-dependent magnetic susceptibility of the quaternary telluride was inspected in a temperature range from 2 to 300 K and in applied fields of up to 10 kOe.

# **Computational Details**

The electronic structure of Rb<sub>3</sub>Er<sub>4</sub>Cu<sub>5</sub>Te<sub>10</sub> was prototypically examined to provide an insight into the bonding situation for this sort of quaternary telluride. Because the crystal structure of Rb<sub>3</sub>Er<sub>4</sub>Cu<sub>5</sub>Te<sub>10</sub> comprises one positionally disordered copper site (Table 2) which is not suited for a starting structure model for the density-functional-theory-based computations, [12b] two models approximating the actual crystal structure of Rb<sub>3</sub>Er<sub>4</sub>Cu<sub>5</sub>Te<sub>10</sub> were used as inputs for the density-functional-theory-based calculations (Supporting Information, Figure S4). Among those models, the "Rb<sub>3</sub>Er<sub>4</sub>Cu<sub>5</sub>Te<sub>10</sub>" model corresponding to the lowest total energy was utilized for the evaluation of the electronic structure, as the model which is linked to the lowest total energy among diverse plausible structure models is the most favorable to be compared to the experimentally determined crystal structure. [21a,c,d,33]

The full structural optimizations, which included lattice parameters as well as atomic positions, and the electronic structure computations were carried out using the projector augmented wave (PAW) method<sup>[34]</sup> within the Vienna ab initio simulation package (VASP).[35] In all computations, correlation and exchange were described by the generalized gradient approximation of Perdew, Burke, and Ernzerhof (GGA-PBE).[36] A Hubbard U parameter that is typically<sup>[37]</sup> used to describe the strong correlations related to the 4f electrons of a given lanthanide atom was not included, because all computations were carried out in nonmagnetic regimes, in which the Er-4f states were treated as core-like. This approach was chosen, because it is still hard to sufficiently [38] describe the strong correlations of 4f electrons of heavier lanthanides, even if a U parameter is taken into consideration. While screenings for appropriate U parameters might help to overcome these issues in certain cases, yet, such approaches are still problematic for lanthanides like erbium. [21b,39] Furthermore, this approach could also be used, because the outcome of the magnetic measurements indicates that the Er-4f electrons are rather localized, and, accordingly, do not contribute to (bonding) states being in the primary focus of the herein presented research. The energy cutoff of the plane wave basis sets was 500 eV, and sets of 3× 3×12 k-points were employed to sample the first Brillouin zones. All calculations were considered to be converged until the energy differences fell below 10<sup>-8</sup> (and 10<sup>-6</sup>) eV/cell between two iterative steps for the electronic (and ionic) relaxations. The AFLOW code[37] was used to generate the coordinates of the high-symmetry k-path in the Brillouin zone, while the electronic band structure of the "Rb $_3$ Er $_4$ Cu $_5$ Te $_{10}$ " model with the lowest total energy was analyzed and visualized with the aid of the Python Materials Genomics (*pymatgen*) program.<sup>[40]</sup>

A (chemical) bonding analysis for the "Rb<sub>3</sub>Er<sub>4</sub>Cu<sub>5</sub>Te<sub>10</sub>" model corresponding to the lowest total energy was accomplished based on the crystal orbital Hamilton population (COHP)[23,41] curves and their integrated values which were computed using the tight-binding linear-muffin-tin-orbital (TB-LMTO) method with the atomic sphere approximation in the Stuttgart code. [42] In the COHP[23,41] approach, the off-site entries of a given density-of-states matrix is weighted by the respective Hamilton matrix elements thereby indicating antibonding, non-bonding, and bonding interactions. The structural parameters of the "Rb<sub>3</sub>Er<sub>4</sub>Cu<sub>5</sub>Te<sub>10</sub>" model which was optimized using the PAW method (see above) were transferred into the TB-LMTO-ASA program with the aid of the wxDragon code. [43] All Wigner-Seitz (WS) radii were generated automatically, and empty spheres were added to accomplish an optimal approximation of full potentials. The following orbitals were employed as basis sets (orbitals treated in the downfolded<sup>[44]</sup> technique are in parentheses): Rb-5s/(-5p)/(-4d)/(-4f); Er-6s/(-6p)/-5d; Cu-4s/-4p/-3d; Te-5s/-5p/(-5d)/(-4f). The respective WS radii (Å) were: Rb, 4.26-4.58; Er, 3.24-3.31; Cu, 2.60-2.67; Te, 3.20-3.26. The erbium 4f states were treated as core-like states - a procedure that has been largely employed in density-functional-theory-based computations on rare-earth-containing (intermetallic) compounds. [21b,33a,45] The reciprocal space integrations were achieved using the tetrahedron method<sup>[46]</sup> with a  $4\times4\times12$  kpoints set.

2108220 (for  $Rb_3Er_4Cu_5Te_{10}$ )Deposition Number 2108220 (for  $Rb_3Er_4Cu_5Te_{10}$ ) contains the supplementary crystallographic data for this paper. These data are provided free of charge by the joint Cambridge Crystallographic Data Centre and Fachinformationszentrum Karlsruhe Access Structures service www.ccdc.cam.ac.uk/structures.

**Supporting Information** (see footnote on the first page of this article): powder X-ray diffraction patterns and Rietveld refinements of Rb<sub>3</sub>Er<sub>4</sub>Cu<sub>5</sub>Te<sub>10</sub>; representation of the crystal structure of K<sub>3</sub>Er<sub>4</sub>Cu<sub>5</sub>Te<sub>10</sub>; representations and total energies of the inspected Rb<sub>3</sub>Er<sub>4</sub>Cu<sub>5</sub>Te<sub>10</sub> models; atom- and orbital-projected DOS curves of the Rb<sub>3</sub>Er<sub>4</sub>Cu<sub>5</sub>Te<sub>10</sub> model corresponding to the lowest total energy; –ICOHP/bond values and distances of selected interactions in the Rb<sub>3</sub>Er<sub>4</sub>Cu<sub>5</sub>Te<sub>10</sub> model corresponding to the lowest total energy.

# **Acknowledgments**

We wish to thank Prof. Dr. R. Dronskowski for valuable advice and the allocation of the computer cluster as well as the lab space, Tobias Storp, Andreas Houben, and Björn Faßbänder for the collections of the sets of single-crystal and powder X-ray diffraction data, respectively, the IT Center at RWTH Aachen University for the granted computer time (JARA-HPC project jara0167), and the Verband der Chemischen Industrie eV (FCI), Frankfurt a. M., Germany, for the financial support (Liebig-Stipend



to ST). Open Access funding enabled and organized by Projekt DEAL.

## Conflict of Interest

The authors declare no conflict of interest.

**Keywords:** Electronic Structure · Intermetallic Phases · Metal-Metal Interactions · Solid-State Reactions · Solid-State Structures

- [1] M. G. Kanatzidis, Inorg. Chem. 2017, 56, 3158-3173.
- [2] a) J. R. Sootsman, D. Y. Chung, M. G. Kanatzidis, Angew. Chem. Int. Ed. 2009, 48, 8616–8639; Angew. Chem. 2009, 121, 8768–8792; b) G. J. Snyder, E. S. Toberer, Nat. Mater. 2008, 7, 105–114.
- [3] a) M. Wuttig, N. Yamada, Nat. Mater. 2007, 6, 824–832; b) D. Lencer, M. Salinga, B. Grabowski, T. Hickel, J. Neugebauer, M. Wuttig, Nat. Mater. 2008, 7, 972–977; c) M. Wuttig, S. Raoux, Z. Anorg. Allg. Chem. 2012, 638, 2455–2465
- [4] M. Z. Hasan, C. L. Kane, Rev. Mod. Phys. 2010, 82, 3045-3067.
- [5] W. S. Sheldrick, Z. Anorg. Allg. Chem. 2012, 638, 2401–2424.
- [6] a) G. J. Miller, Eur. J. Inorg. Chem. 1998, 1998, 523–536; b) R. Nesper, Angew. Chem. Int. Ed. 1991, 30, 789–817; Angew. Chem. 1991, 103, 805– 834.
- [7] a) G. A. Papoian, R. Hoffmann, Angew. Chem. Int. Ed. 2000, 39, 2408–2448; Angew. Chem. 2000, 112, 2500–2544; b) P. Böttcher, Angew. Chem. Int. Ed. 1988, 27, 759–772; Angew. Chem. 1988, 100, 781–794.
- [8] a) E. Zintl, Angew. Chem. 1939, 52, 1–6; b) G. J. Miller, M. W. Schmidt, F. Wang, T.-S. You, Struct. Bond. 2011, 139, 1–55; c) R. Nesper, Z. Anorg. Allg. Chem. 2014, 640, 2639–2648; d) H. Schäfer, B. Eisenmann, W. Müller, Angew. Chem. Int. Ed. 1973, 12, 694–712; Angew. Chem. 1973, 85, 742–760
- [9] a) C. Ertural, S. Steinberg, R. Dronskowski, RSC Adv. 2019, 9, 29821–29830; b) J.-Y. Raty, M. Schumacher, P. Golub, V. L. Deringer, C. Gatti, M. Wuttig, Adv. Mater. 2019, 31, 1806280.
- [10] M. Wuttig, V. L. Deringer, X. Gonze, C. Bichara, J.-Y. Raty, Adv. Mater. 2018, 30, 1803777.
- [11] a) J. Simons, J. Hempelmann, K. S. Fries, P. C. Müller, R. Dronskowski, S. Steinberg, RSC Adv. 2021, 11, 20679–20686; b) J. Hempelmann, P. C. Müller, P. M. Konze, R. P. Stoffel, S. Steinberg, R. Dronskowski, Adv. Mater. 2021, 33, 2100163.
- [12] a) J. D. Corbett, Inorg. Chem. 2010, 49, 13–28; b) F. C. Gladisch, S. Steinberg, Crystals 2018, 8, 80; c) Q. Lin, G. J. Miller, Acc. Chem. Res. 2018, 51, 49–58.
- [13] a) F. C. Gladisch, S. Steinberg, Eur. J. Inorg. Chem. 2017, 2017, 3395–3400; b) K. C. Göbgen, F. C. Gladisch, S. Steinberg, Inorg. Chem. 2018, 57, 412–421; c) K. C. Göbgen, K. S. Fries, F. C. Gladisch, R. Dronskowski, S. Steinberg, Inorganics 2019, 7, 70; d) K. Eickmeier, K. S. Fries, F. C. Gladisch, R. Dronskowski, S. Steinberg, Crystals 2020, 10, 184; e) K. Eickmeier, S. Steinberg, Crystals 2020, 10, 916; f) S. Smid, S. Steinberg, Materials 2020, 13, 2178.
- [14] a) Q. Lin, J. D. Corbett, *Inorg. Chem.* 2011, *50*, 11091–11098; b) S. Gupta, J. D. Corbett, *Inorg. Chem.* 2012, *51*, 2247–2253; c) V. Smetana, Q. Lin, D. K. Pratt, A. Kreyssig, M. Ramazanoglu, J. D. Corbett, A. I. Goldman, G. J. Miller, *Angew. Chem. Int. Ed.* 2012, *51*, 12699–12702; *Angew. Chem.* 2012, *124*, 12871–12874.
- [15] a) M. G. Kanatzidis, R. Pöttgen, W. Jeitschko, Angew. Chem. Int. Ed. 2005, 44, 6996–7023; Angew. Chem. 2005, 117, 7156–7184; b) O. Janka, R. Pöttgen, in: Handbook of Solid State Chemistry (Eds.: R. Dronskowski, S. Kikkawa, A. Stein), Wiley-VCH: Weinheim, Germany, Wiley-VCH: Weinheim, Germany, 2017; c) K. Mitchell, J. A. Ibers, Chem. Rev. 2002, 102, 1929–1952.
- [16] a) F. Q. Huang, J. A. Ibers, J. Solid State Chem. 2001, 160, 409–414;
   b) F. Q. Huang, W. Choe, S. Lee, J. S. Chu, Chem. Mater. 1998, 10, 1320–1326.
- [17] B. Cordero, V. Gómez, A. E. Platero-Prats, M. Revés, J. Echeverría, E. Cremades, F. Barragán, S. Alvarez, *Dalton Trans.* 2008, 2008, 2832–2838.
- [18] a) P. K. Mehrotra, R. Hoffmann, *Inorg. Chem.* 1978, 17, 2187–2189;
   b) K. M. Merz Jr., R. Hoffmann, *Inorg. Chem.* 1988, 27, 2120–2127;
   c) P. Pyykkö, *Chem. Rev.* 1997, 97, 597–636.

- [19] a) D. Prodius, V. Smetana, S. Steinberg, M. Wilk-Kozubek, Y. Mudryk, V. K. Pecharsky, A.-V. Mudring, *Mater. Horiz.* 2017, 4, 217–221; b) H. Lueken, *Magnetochemie*, Vieweg + Teubner Verlag, Stuttgart, Deutschland, 1999.
- [20] L. D. Gulay, D. Kaczorowski, J. Alloys Compd. 2006, 422, 16-20.
- [21] a) I. Bigun, S. Steinberg, V. Smetana, Y. Mudryk, Y. Kalychak, L. Havela, V. Pecharsky, A.-V. Mudring, Chem. Mater. 2017, 29, 2599–2614; b) S. Steinberg, N. Card, A.-V. Mudring, Inorg. Chem. 2015, 54, 8187–8196; c) S. Steinberg, R. P. Stoffel, R. Dronskowski, Cryst. Growth Des. 2016, 16, 6152–6155; d) R. Gautier, X. Zhang, L. Hu, L. Yu, Y. Lin, T. O. L. Sunde, D. Chon, K. N. Poeppelmeier, A. Zunger, Nat. Chem. 2015, 7, 308–316.
- [22] a) S. Steinberg, J. Brgoch, G. J. Miller, G. Meyer, *Inorg. Chem.* 2012, 51, 11356–11364; b) K. C. Göbgen, S. Steinberg, R. Dronskowski, *Inorg. Chem.* 2017, 56, 11398–11405.
- [23] S. Steinberg, R. Dronskowski, Crystals 2018, 8, 225.
- [24] F. A. Cotton, G. Wilkinson, *Anorganische Chemie*, Verlag Chemie, Weinheim, Deutschland, **1974**.
- [25] SAINT + and SADABS, versions 7.68 and 2004/1, Bruker AXS Inc., Madison, WI. USA, 2009.
- [26] APEX2 v2014.11-0, Bruker Nonius, Bruker AXS Inc., Madison, WI, USA, 2003, 2004, 2005–2014.
- [27] a) G. M. Sheldrick, Acta Crystallogr. Sect. A 2008, 64, 112–122; b) G. M. Sheldrick, Acta Crystallogr. Sect. C 2015, 71, 3–8.
- [28] A. L. Spek, Acta Crystallogr. Sect. D 2009, 65, 148–155.
- [29] WinXPow, 2.23 ed., STOE & Cie GmbH, Darmstadt, Germany, 2005.
- [30] H. Putz, Match!, version 3.6.1.115, Crystal Impact GbR, Bonn, Germany, 2018.
- [31] J. Rodriguez-Carvajal, Physica B: Condensed Matter 1993, 192, 55-69.
- [32] T. Roisnel, J. Rodriguez-Carvajal, in Proceedings of the Seventh European Powder Diffraction Conference (EPDIC 7) (Eds.: E. Delherz, E. J. Mittenmeijer), 2000, pp. 118–123.
- [33] a) V. Smetana, S. Steinberg, Y. Mudryk, V. Pecharsky, G. J. Miller, A.-V. Mudring, *Inorg. Chem.* 2015, 54, 10296–10308; b) F. Wang, K. N. Pearson, G. J. Miller, *Chem. Mater.* 2009, 21, 230–236.
- [34] P. E. Blöchl, *Phys. Rev. B: Condens. Matter Mater. Phys.* **1994**, 50, 17953–17979.
- [35] a) G. Kresse, M. Marsman, J. Furthmüller, Vienna Ab Initio Simulation Package (VASP), The Guide, Computational Materials Physics; Faculty of Physics, Universität Wien: Vienna, Austria, 2014; b) G. Kresse, J. Furthmüller, Comput. Mater. Sci. 1996, 6, 15–50; c) G. Kresse, J. Furthmüller, Phys. Rev. B: Condens. Matter Mater. Phys. 1996, 54, 11169– 11186; d) G. Kresse, J. Hafner, Phys. Rev. B: Condens. Matter Mater. Phys. 1993, 47, 558–561; e) G. Kresse, D. Joubert, Phys. Rev. B: Condens. Matter Mater. Phys. 1999, 1758–1775.
- [36] J. P. Perdew, K. Burke, M. Ernzerhof, Phys. Rev. Lett. 1996, 77, 3865–3868.
- [37] W. Setyawan, S. Curtarolo, Comput. Mater. Sci. 2010, 49, 299–312.
- [38] W.-L. Li, C. Ertural, D. Bogdanovski, J. Li, R. Dronskowski, *Inorg. Chem.* 2018, 57, 12999–13008.
- [39] K. Tao, J. Zhou, Q. Sun, Q. Wang, V. S. Stepanyuk, P. Jena, *Phys. Rev. B: Condens. Matter Mater. Phys.* 2014, 89, 085103.
- [40] S. P. Ong, W. D. Richards, A. Jain, G. Hautier, M. Kocher, S. Cholia, D. Gunter, V. L. Chevrier, K. A. Persson, G. Ceder, Comput. Mater. Sci. 2013, 68, 314–319.
- [41] R. Dronskowski, P. E. Blöchl, J. Phys. Chem. 1993, 97, 8617–8624.
- [42] a) R. Tank, O. Jepsen, A. Burkhardt, O. K. Andersen, *TB-LMTO-ASA Program, version 4.7*, Max-Planck-Institut für Festkörperforschung: Stuttgart, Germany, 1994; b) O. K. Andersen, O. Jepsen, *Phys. Rev. Lett.* 1984, 53, 2571–2574.
- [43] B. Eck, wxDragon 2.1.6, RWTH Aachen University: Aachen, Germany, 2018.
- [44] W. R. L. Lambrecht, O. K. Andersen, Phys. Rev. B: Condens. Matter Mater. Phys. 1986, 34, 2439–2449.
- [45] a) P. Chai, J. D. Corbett, *Inorg. Chem.* 2011, *50*, 10949–10955; b) P. Chai,
   J. D. Corbett, *Inorg. Chem.* 2012, *51*, 3548–3556; c) S. Steinberg, T. Bell,
   G. Meyer, *Inorg. Chem.* 2015, *54*, 1026–1037.
- [46] P. E. Blöchl, O. Jepsen, O. K. Andersen, Phys. Rev. B: Condens. Matter Mater. Phys. 1994, 49, 16223–16233.

Manuscript received: September 8, 2021 Revised manuscript received: October 4, 2021 Accepted manuscript online: October 6, 2021